International Journal of Fatigue 201 (2025) 109189

Contents lists available at ScienceDirect

International Journal of Fatigue

journal homepage: www.elsevier.com/locate/ijfatigue

Enhancing fatigue performance of austenitic stainless steel via warm surface severe plastic deformation using surface mechanical attrition treatment

Y Austernaud [a,b,c,*], M Novelli [a,b,*], T Grosdidier [a,b], P Bocher [c]

[a] Laboratoire d'Etude des Microstructures et de Mécanique des Matériaux (LEM3), UMR CNRS 7239, 7 rue Félix Savart, BP 15082, Metz F-57073, France
[b] LABoratoire d'Excellence Design des Alliages Métalliques pour Allègement des Structures (DAMAS), Université de Lorraine, Metz F-57045, France
[c] Laboratoire d'Optimisation des Procédés de Fabrication Avancés (LOPFA), Ecole de technologie supérieure, 1100 rue Notre Dame Ouest, H3C 1K3 Montréal, Canada

ARTICLE INFO

Keywords:
Austenitic stainless steel
Surface severe plastic deformation (SSPD)
Surface mechanical attrition treatment (SMAT)
Residual stress relaxation
Fatigue
Ultrasonic shot peening (USP)

ABSTRACT

The effects of warm Surface Severe Plastic Deformation (SSPD) performed via Surface Mechanical Attrition Treatment (SMAT) on the microstructure, hardness, and residual stress gradients, as well as the resulting fatigue properties of a 316L austenitic stainless steel were investigated. Machined samples were ultrasonically shot peened for 10 min at Room Temperature (RT), 523 K, and 773 K before undergoing rotating-bending fatigue tests to determine the endurance limit. The RT-SMATed sample, for which machining grooves are removed by the shot impacts, showed a superior fatigue limit endurance than machined samples (+25 %), with subsurface nucleation sites. The 523 K peened samples revealed a similar fatigue limit endurance accompanied by the same type of subsurface crack nucleation. Due to the increased roughness and expansion of surface stress raisers by pile-ups and surface oxidation, the nucleation of the fatigue cracks occurred at the extreme surface when SMAT was done at 773 K. Despite the surface nucleation, SMAT carried out at 773 K provided a superior endurance limit (+15 % compared to RT-SMAT). This improvement was attributed to the restored microstructure formed under 773 K peening, which stabilizes the introduced compressive residual stress, and to the deeper and lower tensile peak induced by warm SMAT. To support the interpretation of fatigue behaviour under varying mean stress conditions, a Goodman analysis was conducted, confirming the beneficial role of compressive residual stress introduced by warm peening on endurance limit improvement.

1. Introduction

Industry requires increasingly high-performance parts with enhanced mechanical properties. The surface of mechanical components generally plays an important role in mechanical performance, especially in fatigue failures. Indeed, surface imperfections often create stress concentrations which represent privileged location for the nucleation of fatigue cracks. Consequently, surface roughness is a factor that influences the fatigue behaviour of metals [1,2]. On the other hand, the presence of residual stress can significantly affect the crack nucleation and propagation behaviour [3]. Compressive Residual Stress (CRS) is advantageous for enhancing the resistance to fatigue because it delays the nucleation of cracks and reduces their rate of propagation through crack closure [4,5]. The microstructural state of the material is also important as nanograins and ultrafine grains are known to improve the high cycle fatigue resistance thanks to the higher strength of the material. On the other hand, a decrease in the low cycle resistance can be observed due to the associated loss in ductility [6,7].

Processes such as Shot Peening (SP) are widely used to introduce CRS at the material surface, and improve thereby fatigue properties [8–10]. Severe Shot Peening (SSP) which consist in the projection of shots at high velocity for a fairly long time has also been used because it enables to significantly refine the microstructure [11]. One of the possible drawbacks of SSP is over-shot peening which can generate surface defects, or short cracks acting as stress raisers [11], thereby considerably reducing the fatigue performance of the treated part.

Derived versions of severe shot peening have been developed, such as Surface Mechanical Attrition Treatment (SMAT) also referred as

* Corresponding authors at: Laboratoire d'Etude des Microstructures et de Mécanique des Matériaux (LEM3), UMR CNRS 7239, 7 rue Félix Savart, BP 15082, Metz F-57073, France.
E-mail addresses: yann.austernaud@univ-lorraine.fr (Y. Austernaud), marc.novelli@univ-lorraine.fr (M. Novelli).

https://doi.org/10.1016/j.ijfatigue.2025.109189
Received 26 May 2025; Received in revised form 18 July 2025; Accepted 21 July 2025
Available online 22 July 2025

Ultrasonic Shot Peening (USP), in which the shots are given a wide range of rather random trajectories within a confined chamber to enhance the microstructural refinement [12,13]. This process generates Surface Severe Plastic Deformation (SSPD) with less risk of generating stress raisers by over-peening [14,15]. SMAT is a multiparametric process where treatment parameters such as the peening duration and the shot velocity affect the gradients introduced into the material [16,17], as well as the surface integrity [18], and consequently, the fatigue resistance [19,20]. Another factor influencing the microstructural gradients and potentially affecting fatigue properties is the temperature at which the severe plastic deformation is imparted. While the effect of decreasing the SMAT temperature down to a cryogenic level, has been investigated in terms of martensitic transformation [21] and improvement of the fatigue limit of metastable alloys [22]. The effect of warm SMAT was only documented for the microstructure evolution of a 316L steel [23] and the effect of warm SMAT on fatigue was only tested on a NiTi alloy [24]. For this alloy an increase in fatigue resistance after warm SMAT was obtained compared to the untreated condition, although no comparison was made with SMAT carried out at Room Temperature (RT).

Austenitic stainless steels (ASSs) are widely used in the industry due to their good corrosion resistance and they are particularly well suited for SMAT due to their excellent work hardening ability. Applying SMAT to ASS has improved the fatigue resistance by nearly 30 % by delaying crack nucleation [25,26]. The 316L is a particularly relevant ASS as it can be strengthened by SSPD and several studies have reported the benefit of RT-SMAT in terms of microstructure gradients residual stress gradients [16,27], and fatigue properties [25,28]. In a recent study, warm SMAT was investigated on a recrystallized 316L, it was shown that controlling the peening temperature allowed to drastically modify the mechanisms accommodating the deformation and the nature of the gradient microstructures [23].

This study aims to investigate the effect of thermomechanical deformations induced by SMAT on the microstructural modifications on an as-drawn 316L. This study will document the surface and microstructural modifications brought by SMAT at room temperature, 523 K and 773 K. The fatigue performance of the SMATed sample will be tested through 4-points rotating bending fatigue. The evolution of the residual stress with the number of cycles will be documented and the potential benefit of controlling the process temperature will be clarified to establish the relationship between process temperature, microstructure, and mechanical performance.

2. Materials and methods

2.1. Material and peening treatment

The investigated material is a 316L austenitic stainless steel in a work-hardening state, drawn to a Ø12.7 mm cylindrical bars. Cylindrical specimens were machined from these rods in 6 mm gauge diameter samples with a gauge length of 25 mm as shown in Fig. 1. The material had an initial hardness of 345 ± 5 HK (corresponding to 320 $HV_{0.02}$), reflecting its work-hardened state. This condition, as opposed to the recrystallized one used to investigate the effect of warm SMAT on microstructure evolution mechanisms [23], was selected as it is more representative of the metallurgical state used in industrially manufactured components. The initial microstructure is characteristic of cold drawn material deformation with elongated grains containing mechanical twins and internal grain disorientation. An Electron Back Scatter Diffraction (EBSD) map of the initial microstructure is provided in Fig. 2 in the transverse direction of the cylindrical specimen (XZ plane, as indicated in Fig. 1). No martensite phase was documented.

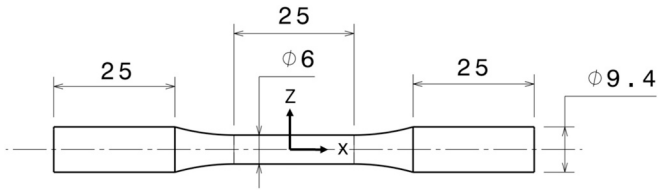

Fig. 1. Fatigue specimen geometry (in mm).

SMAT processing was carried out for 10 min on cylindrical specimens with a sonotrode amplitude of 60 µm, a frequency of 20 kHz, and Ø2 mm 100C6 shots. Only the temperature was set as a treatment variable with SMAT performed at RT, 523 K and 773 K. The samples were heated from the top by a focused heating lamp while the peening took place at the bottom. During the treatment, the cylindrical sample (Fig. 1) was rotated at 10 rpm. More details about the process are given in a previous study [23].

2.2. Evaluation of the fatigue properties

The fatigue tests were done on a R.R. Moore 4-points rotating bending fatigue machine (R = −1) with a rotating frequency of 20 Hz. The fatigue endurance was estimated following the STEP method [29], fixing the endurance limit to 10^6 cycles for each SMAT condition. Some fatigue tests carried out under a stress amplitude (σ_a) of 500 MPa and 600 MPa were interrupted to measure the surface residual stress after different cycling numbers: 1,10^1,10^2, 10^3,10^4,10^5,10^6.

2.3. Surface and subsurface characterizations

Roughness was measured with a Mitutoyo SJ-400 profilometer with a cutoff λ_c of 2.5 mm and an evaluation length set at 12.5 mm, following ISO 4287. Table 1 gives mean values and standard deviations based on 10 measurements of the surface roughness parameters R_a, R_q, R_t, and R_{sm}. R_a is the arithmetic average roughness, Rq the root mean square roughness, R_t is the vertical distance between the highest peak and deepest valley over the entire evaluation length, and R_{sm} is the mean spacing between successive peaks within the sampling length. The corresponding stress concentration factor K_t, which estimates the increase in local stress induced by the surface roughness of each condition, was calculated using an equation from finite element simulations of Li et al. [30] for rough surfaces, as:

$$K_t = 1 + 4.0\left(\frac{R_t}{R_{sm}}\right)^{1.3} \quad for \quad \left(\frac{R_t}{R_{sm}}\right) < 0.15 \tag{1}$$

Surface characterizations were performed using a Hirox optical microscope and a Zeiss SUPRA 40 Scanning Electron Microscope (SEM). Hardness gradients were measured using Knoop microhardness indentations with a Clemex JS2000 microhardness tester. A constant load of 100 gf and a dwell time of 10 s were applied for all measurements.

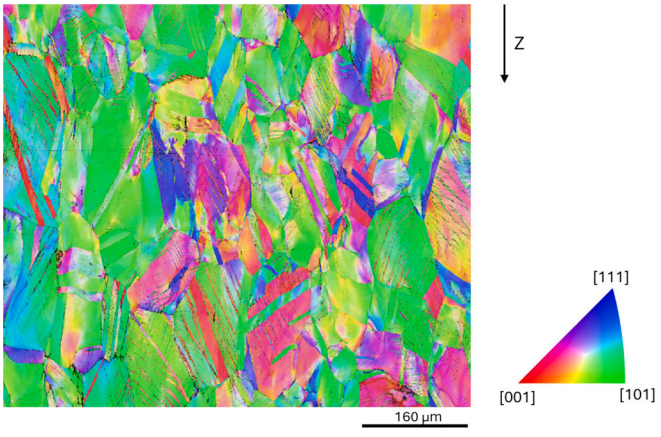

Fig. 2. EBSD map of the initial microstructure (XZ plane in Fig. 1) represented in Inverse Pole Figure (IPF) colour on the Z-axis.

Table 1
Mean roughness values and corresponding stress concentration factors for the different treatment conditions. Error values represent ± 1 standard deviation from the mean value (n = 10).

Surface treatment	As machined	RT-SMAT	523 K-SMAT	773 K-SMAT
R_a [µm]	1.4 ± 0.1	2.5 ± 0.2	3.6 ± 0.3	4.1 ± 0.4
R_q [µm]	1.7 ± 0.2	3.1 ± 0.2	4.4 ± 0.4	5.0 ± 0.5
R_t [µm]	9.1 ± 1.2	17.3 ± 2.6	25.9 ± 5.1	28.3 ± 3.6
R_{sm} [µm]	70 ± 7	810 ± 136	699 ± 67	706 ± 88
K_t	3.1	2.1	2.4	2.4

Indentations were initiated at a depth of 25 µm from the treated surface and continued towards the core in increments of 25 µm. Surface hardness was determined through direct indentation on the sample surface. At each depth, the mean hardness values and standard deviations were calculated based on five measurements.

Residual stress was measured based on the cos (α) method [31] using a Pulstec µ360 X-ray diffraction instrument with a tension of 30 kV, a current of 1.5 mA and a chromium source with an incidence β angle of 30°. The acquisitions were carried out on the specimen axial direction (along the X-axis in Fig. 1) and the calculations were made on the $\{311\}_\gamma$ austenite (Cr-K_β = 2.085 Å). Residual stress gradients were acquired by successive electropolishing matter removals using an A3 solution (5 % perchloric acid, 60 % methanol and 35 % butoxyethanol), then the removed depths were measured using a contact profilometer. From the surface down to approximately 150 µm depth, measurements were performed roughly every 20 µm, depending on the amount of material removed by electropolishing. Beyond 150 µm depth, measurements were taken approximately every 50 µm, depending on the electropolishing material removal. A correction was applied to account for the stress relaxation induced by matter removal using the method proposed by Moore and Evans [32] for cylindrical bars. Values and related error bars given in the article are the mean values and the standard deviations calculated on 5 measurements made at different locations on the specimen gauge section circumference.

For the microstructural observations, samples were mirror-polished using 320 SiC paper down to OPS before electronic imaging. The microstructures were investigated on cross-sections by SEM imaging under Back Scattered Electron (BSE) contrast as well as EBSD using respectively a Zeiss SUPRA 40 and a Jeol F100 SEMs. EBSD maps were acquired with a 50 nm step size using a 15 kV acceleration tension. The EBSD maps were then post-treated with the ATEX software [33].

3. Results

3.1. Surface characteristics

The evolution of the surface morphology is illustrated in Fig. 3 through roughness measurements and surface observations. SMAT generates a higher roughness compared to the as-machined sample with the increase of both R_a and R_q. The initial low R_q value of 1.7 ± 0.2 µm rises by 88 % to 3.1 ± 0.2 µm after RT-SMAT treatment. As SMAT temperature increases, the roughness also increases with R_q reaching 4.4 ± 0.3 µm at 523 K and 5.0 ± 0.5 µm at 773 K (Fig. 3a).

The as-machined specimens present V-shape machining grooves (Fig. 3b) with a width of about 70 µm (R_{sm}) and 9.1 µm depth (R_t) (Table 1) resulting in an associated K_t of 3.1. Optical images of the top surface as a function of the SMAT temperature show that the machining marks are progressively replaced by a cratering pattern typical of the topology of shot peened surfaces (Fig. 3c) decreasing the K_t down to 2.1. The surface of the 773 K-treated sample (Fig. 3d) exhibits a pronounced oxidation state, appearing with a rather bluish shade. Additionally, SEM image (Fig. 3e) highlights material pile-up (red arrows) and surface cracks (red circles), indicating an alteration of the surface integrity by warm SMAT, although the calculated K_t only increases to 2.4. The presence of surface cracks at the surface of the 773 K sample can appear to be in contradiction with the idea that the elevated temperature increases the material ductility. In fact, these surface cracks originate from the fragmentation of some brittle oxide layers that formed at the sample surface.

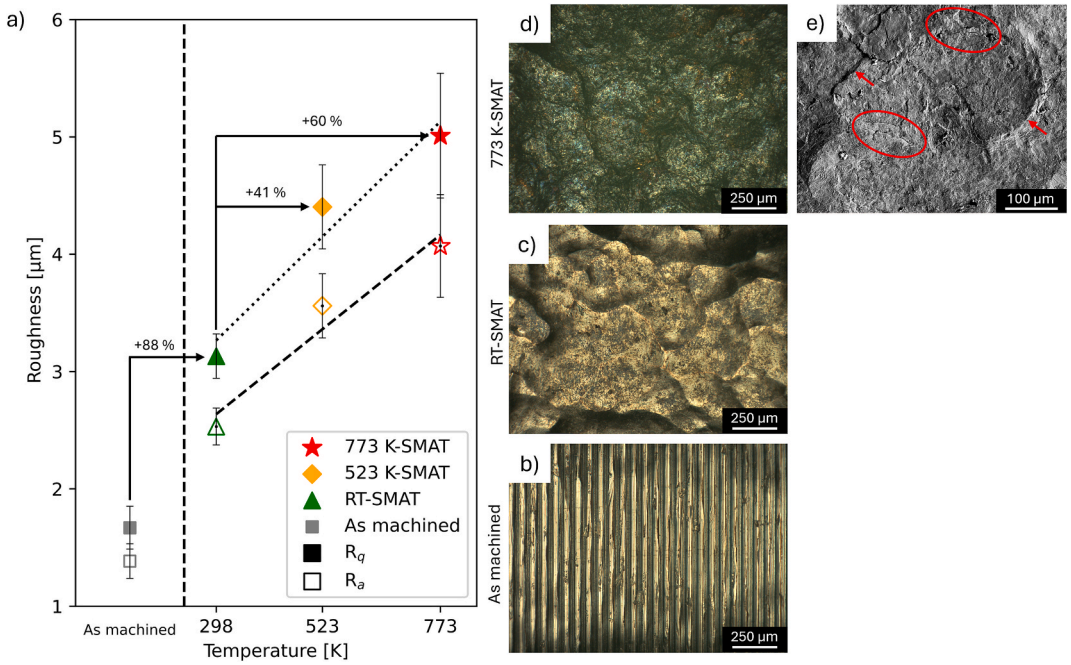

Fig. 3. a) R_a and R_q roughness evolution as a function of the SMAT temperature, optical images of b) as-machined, c) RT-SMATed, d) 773 K-SMATed sample surfaces, and e) SEM image of the 773 K sample showing material pile up (red arrows) and surface cracks (red circles). Error bars represent ± 1 standard deviation from the mean value (n = 10).

3.2. Subsurface gradient structure

The microstructural gradients generated by the SMAT at different temperatures are shown in Fig. 4 through SEM and EBSD images, The SEM images in Fig. 4a-c reveal that, compared to the microstructure of the drawn material (Fig. 2), smaller microstructures are formed near the surface as the initially deformed grains become increasingly fragmented into ultrafine grains (UFG) within the surface region. As a result, the thickness of the SMAT-affected microstructural region increases with increasing temperature.

The EBSD maps in Fig. 4d-f highlight the dependence of the UFG layer thickness on the SMAT temperature. The surface of the RT-SMATed sample in Fig. 4d shows an extremely refine structure extending only on the first two microns and, below this depth, planar defects are found in the initial grains, without the formation of α' martensite (<1%). For the 523 K-SMATed sample (Fig. 4e), the UFG thickness is about 10 μm and, below this depth, a duplex structure with both refined and deformed grains is formed. Dynamic recrystallization process [23] is expected to control the grain refinement at 773 K, resulting in the formation of an UFG layer as thick as approximately 30 μm (Fig. 4f). Thus, globally, warm SMAT leads to an increase in the thicknesses of (i) the ultrafine grain layer and (ii) the overall affected depth.

The evolution of the hardness gradients for the different SMAT temperatures is shown in Fig. 5. The highest hardness values are observed at the surfaces, followed by a gradual decrease until reaching the initial hardness of the core of the specimens (345 ± 5 HK). In the case of RT-SMAT, the surface hardness reaches 427 HK, indicating a + 24 % increase compared to the core hardness. When SMAT is performed at 523 K even higher surface value with the hardness of 450 HK (+30 %) is obtained. Comparatively, only an increase up to 390 HK (+13 %) is reached for the 773 K sample. Fig. 5 also indicates that the SMAT temperature has an impact on the depth of the modified hardness. The initial core hardness is reached at a depth of 200 μm for the sample SMATed at RT, and about 250 μm for both the 523 K and 773 K conditions.

The in-depth residual stress profiles generated by SMAT at the three different temperatures are shown in Fig. 6. For all the samples, a high CRS state (between −660 and −480 MPa) is introduced within the surface area compared to as-machined samples where residual stress of

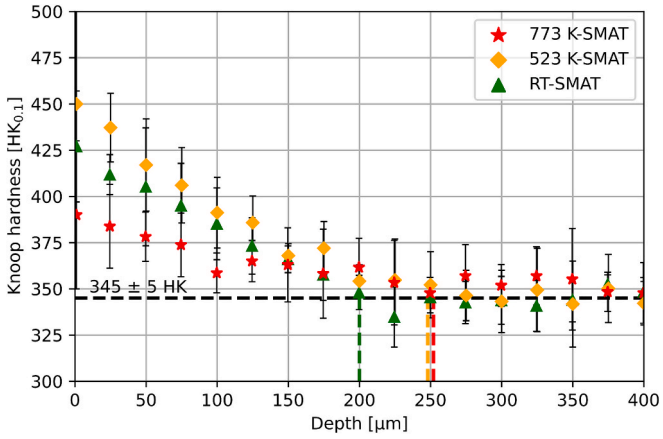

Fig. 5. Hardness evolution along sample depth for SMAT performed at RT (green) 523 K (orange) and 773 K (red). The horizontal dashed line at 345 HK represents the initial hardness of the material. Error bars represent ± 1 standard deviation from the mean value (n = 5).

−60 MPa ± 35 MPa was measured. SMAT done at RT generated a maximum CRS of −780 MPa, located approximately 50 μm beneath the surface. The CRS then decreases sharply with depth, stabilizing around −500 MPa between 120 μm and 200 μm. Beyond this plateau, the CRS gradually transitions into the tensile domain. For the warm peened conditions, a lower magnitude of CRS is observed near the surface, with values of about −620 MPa and −560 MPa at a 50 μm depth for the 523 K and 773 K samples, respectively. For these conditions, CRS forms a plateau with a variation of ± 100 MPa, extending down to a 200 μm depth. Consequently, at a depth of 200 μm and further down within the depth of the material, the CRS values have higher magnitudes than the ones introduced by the cold peening. Thus, the main effect of elevating the temperature of peening is to deepen the plateau of CRS in the subsurface area. For example, CRS of −530 MPa are still present at 250 μm depth under the surface for the 773 K-SMAT while for a RT treatment they are present only over a depth of 150 μm.

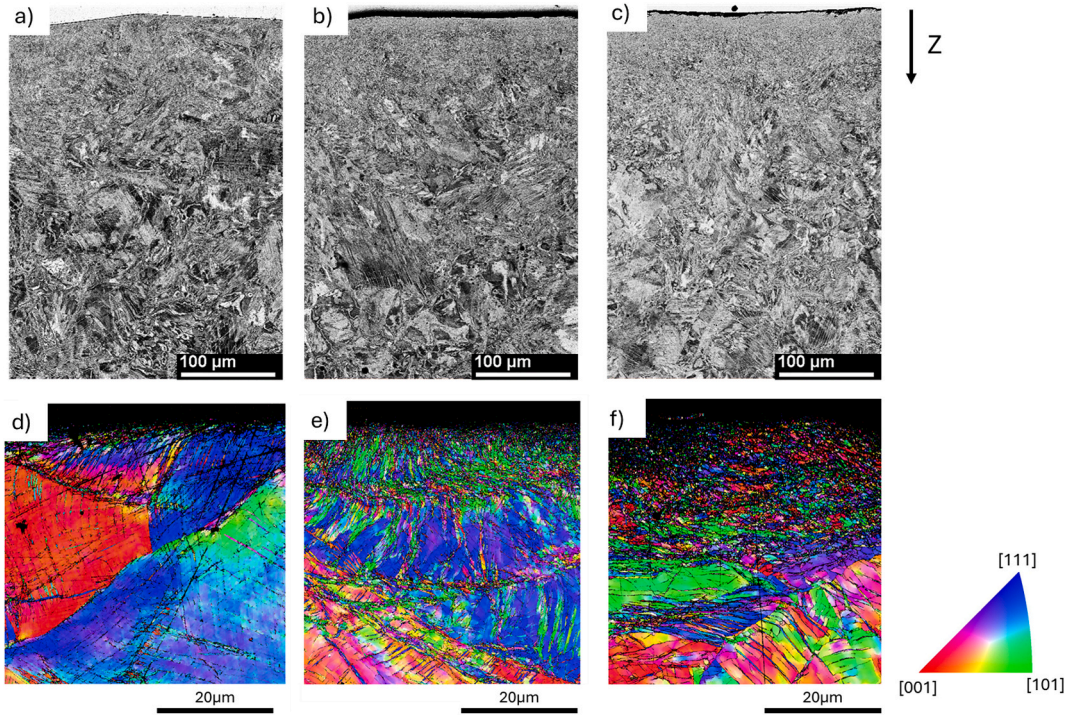

Fig. 4. Cross-section BSE images associated with higher magnification IPF maps along the Z-axis for the specimens SMATed at a, d) RT, b, e) 523 K, and c, f) 773 K.

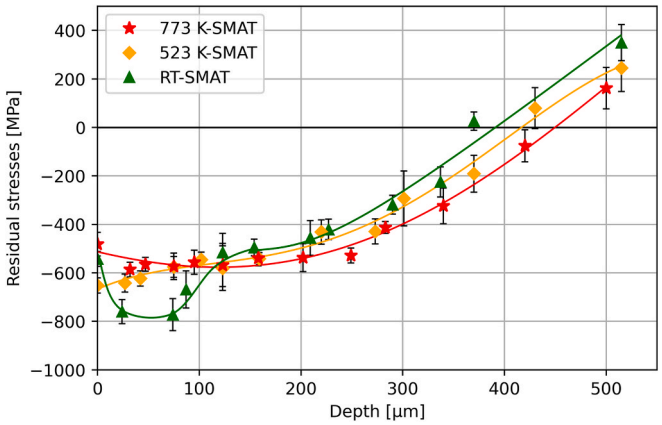

Fig. 6. Residual stress gradients as a function of the sample depth for the sample SMATed at: RT (green), 523 K (orange), and 773 K (red). Error bars represent ± 1 standard deviation from the mean value (n = 5).

3.3. Fatigue behaviour and crack nucleation

The fatigue test results are shown in Fig. 7, illustrating the relationship between stress amplitude and number of cycles to failure for the various peening treatment conditions. The run-out samples are represented by arrow markers, the filled markers indicate the samples in which subsurface crack nucleation sites were observed, while the hollow markers indicate surface crack nucleation sites. The black stars markers correspond to the samples for which fracture surfaces were selected to be displayed in Fig. 8.

The beneficial effect of SMAT temperature on the fatigue life of the 316L varies depending on fatigue life range; being more pronounced in the high cycle fatigue regime than in the low cycle one. In all cases the SMAT conditions result in an increase of the fatigue limit compared to the as-machined material. The fatigue behaviour of the RT and 523 K-SMATed samples is rather close, with a fatigue endurance limit around 500 MPa, i.e. + 25 % compared to the as-machined condition (400 MPa). For the samples peened at 773 K, the endurance limit is improved by an additional 15 % (575 MPa) compared to those SMATed at RT and 523 K, even though a wide variation in fatigue life is observed under the same loading conditions at this temperature.

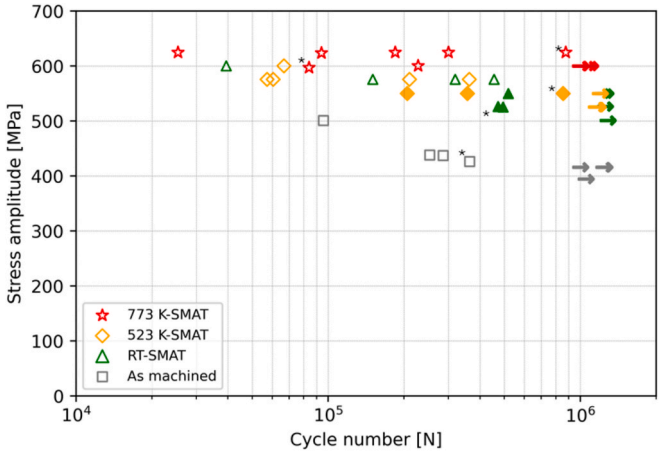

Fig. 7. S-N curves of samples SMATed under the different conditions: as-machined samples (gray squares), RT-SMAT treated samples (green triangles), 523 K-SMAT treated samples (orange diamonds), and 773 K-SMAT treated samples (red stars). Arrows symbolize the run-out samples, hollow markers represent surface crack nucleation sites, and filled markers represent subsurface crack nucleation sites. Black stars indicate the samples used for fractography shown in Fig. 8.

Images from the fractography analysis are gathered in Fig. 8. As was indicated in Fig. 7 by different hollow or filled markers, some clear trends in the fracture crack nucleation can be observed: surface crack nucleation and subsurface crack nucleation. In the case of the as-machined samples, fatigue cracks were always initiated at the surface, on a machined groove. For the SMATed conditions at RT and 523 K, crack nucleation generally occurred in the subsurface area for high cycle numbers (close to 10^6 cycles, filled markers in Fig. 7) while multiple surface cracks nucleation sites are observed for low cycle numbers (hollow markers). When SMAT was carried out at 773 K the nucleation sites were systematically found at the surface of defects formed by SMAT (valley of a crater or pile up).

Fig. 8 I gives the example of a sample with multiple fatigue nucleation sites on a machined sample (Fig. 8 I b,c,d). The fatigue nucleation sites are located at a machining groove where tool marks are present. In the examples given in Fig. 8 II a,b and Fig. 8 III a,b the nucleation sites were located at depths around 400 µm and 450 µm for the RT and 523 K peened samples, respectively. These depths correspond to the depth at which no more compressive residual stress is present. Higher magnification images, show metallurgical crack nucleation sites, without any detected inclusion (Fig. 8 II c,d and III c).

Interestingly, when the SMAT was carried out at 773 K (Fig. 8 IV a-d) the nucleation sites shifted back to the surface area. Fig. 8 IVa, illustrates that multiple surface cracks nucleation sites were generally revealed for the low cycle fatigue sample. Comparatively, only a single crack nucleates in the high cycle regime (Figure IV b). At this temperature, as shown by the higher magnification image (Fig. 8 IV f), the nucleation site is located in a pile-up (crater) formed under the SMAT. The cross-section of the 773 K-SMATed sample prior to fatigue (Fig. 8 IV e) shows the presence of oxide contaminants, heterogeneously distributed across the surface and penetrating to a depth of approximately 5 µm. The oxide layer formed during SMAT can also be observed at the sample surface (Fig. 8 IV f). The fracture surface near the crack initiation site in the samples processed at 773 K do not display microstructural features that could suggest a sort-crack behavior regime. It appears mostly perpendicular (≈90°) to the loading direction. This could be due to the relatively small size of the microstructure around these sites. The pronounced surface oxidation and roughness hindered detailed observation of possible secondary cracks, limiting the ability to track short crack propagation.

Fig. 8 I a II a III a IV a-b are optical view of the fracture surfaces, Fig. 8 I b-d IIb-d III b-c and IV c-d,f show higher magnification SEM images of the crack nucleation sites. Fig. 8e illustrates the presence of oxide contamination on the sample surface, extending to a depth of up to 5 µm after the 773 K treatment.

3.4. Stress relaxation during fatigue

To evaluate the possible relaxation of residual stress occurring during fatigue, interrupted fatigue tests were performed at 500 MPa and 600 MPa with measurements taken before cycling and at various intervals1,10^1,10^2, 10^3,10^4,10^5,10^6 cycles, as well as after sample failure. Residual stress relaxation was evaluated only at the sample surface where the applied stress is maximal and where stress redistribution is expected to occur more readily. Fig. 9a and b compare the evolution of relative residual stress relaxation with the initial residual stress values before cycling for loadings of 500 MPa and 600 MPa, respectively.

For the loading of 500 MPa (Fig. 9a) small drops in residual stress are observed just after the very first fatigue cycle for the lower peening temperature conditions of RT and 523 K. Comparatively, no such decrease in residual stress is observed for the SMAT-treated sample at 773 K. After the first cycle, the residual stress remains rather stable until 10^6 cycles for all peening processed conditions. The residual stress relaxation is more pronounced at 600 MPa (Fig. 9b). Similarly to the stress level at 500 MPa, the RT and the 523 K-SMATed samples exhibit a drop of CRS after the first fatigue cycle with a relaxation of about 70 MPa

and 25 MPa, respectively. Subsequently, a rather limited relaxation is observed in the RT sample until 100 cycles reaching about 80 MPa for an achieved value of CRS about −480 MPa. After 100 cycles, the residual stress relaxes significantly more until the failure of the sample at 39,434 cycles. The residual stress on the postmortem sample is around −170 MPa corresponding to a relaxation of 370 MPa compared to the CRS value before cycling. For the 523 K-SMATed sample, the CRS gradually decrease up to 10^4 cycles reaching 100 MPa of relaxation. Then a major residual stress relaxation happens between 10^4 and 5.10^4 cycles to about 200 MPa. The sample failure occurs quickly after 66,791 cycles and the residual stress values measured on the postmortem sample are around −340 MPa – corresponding approximately to 260 MPa of relaxation. For the 773 K-SMATed sample, no major stress relaxation is measured until 10^5 cycles (except a slight relaxation of 40 MPa between 100 and 1000 cycles). The sample failed at 227,519 cycles with a residual stress level of around −370 MPa, representing a residual stress relaxation of only 125 MPa from the uncycled sample. These results clearly indicate that warm SMAT enables the stabilization of the CRS introduced during peening.

4. Discussion

The effect of SMAT temperature on the fatigue performance of 316L austenitic stainless steel is closely linked to its influence on residual stress gradients and microstructural evolution. At elevated temperatures, the reduction in flow stress facilitates deeper plastic deformation, leading to the formation of deeper gradients. The raise in temperature also increases surface roughness, as the softer material becomes more prone to plastic deformation. However, despite this increased roughness, shot impacts only increase the K_t slightly because the craters formed at higher temperatures are both wider and deeper. These SMAT-induced modifications influence the crack nucleation mechanisms, with both surface and subsurface nucleation observed depending on the treatment temperature.

The following discussion first examines the influence of SMAT temperature on crack nucleation mechanisms, followed by an analysis of the stability of CRS under cyclic loading, and finally addresses the relevance of a Goodman-type diagram to interpret the fatigue performance after SMAT at different temperatures.

4.1. *Effect of SMAT temperature on fatigue performance: modification of crack nucleation sites*

In the as-machined condition, cracks nucleated at surface machining grooves (Fig. 8 I) that acted as stress concentrators. These grooves, characterized by V-shapes with depths of 9.1 μm and widths of 70 μm (Fig. 3, Table 1), created significant stress raisers estimated with a K_t of 3.1 (Table 1). The presence of stress raisers with limited CRS at the surface (−60 MPa) facilitated surface cracks nucleation at these notches, as documented by the fractography results (Fig. 8 I c,d).

By carrying out SMAT at RT and 523 K, the mechanism of crack nucleation shifted from the surface to the subsurface in the high cycle regime (at low stress levels). Fatigue endurance is improved by approximately 25 % compared to the as-machined sample (Fig. 7) after SMAT at RT and 523 K. The mechanical grooves are replaced by shot-induced craters with depths of 17.3 μm and 25.9 μm, and widths of 810 μm and 699 μm, for the RT and 523 K-SMAT conditions, respectively. As a result, K_t decreases to 2.1 and 2.4 (Table 1), while CRS exceeded −500 MPa in both cases (Fig. 6). The introduction of these large CRS prevents surface crack nucleation and shifts the crack

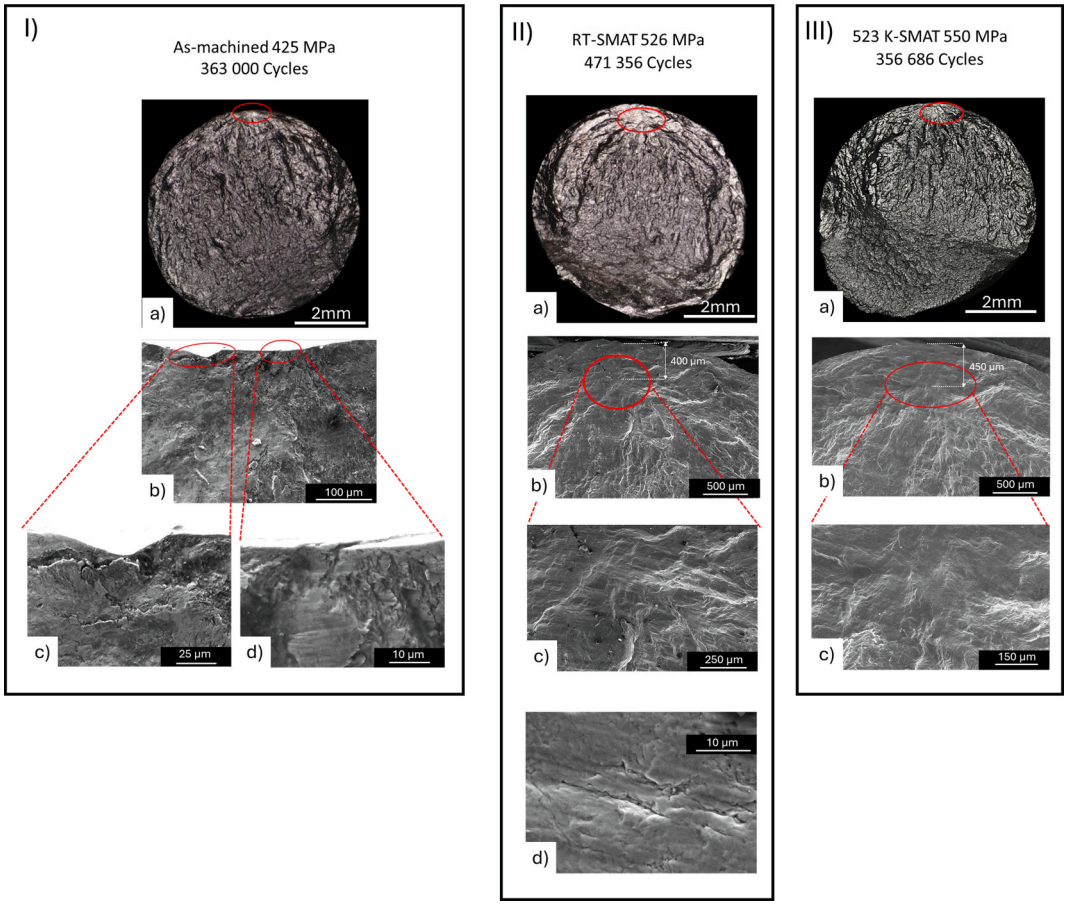

Fig. 8. Fractography of samples: I) as-machined; II) RT-SMAT; III) 523 K-SMAT; and IV) 773-K SMAT.

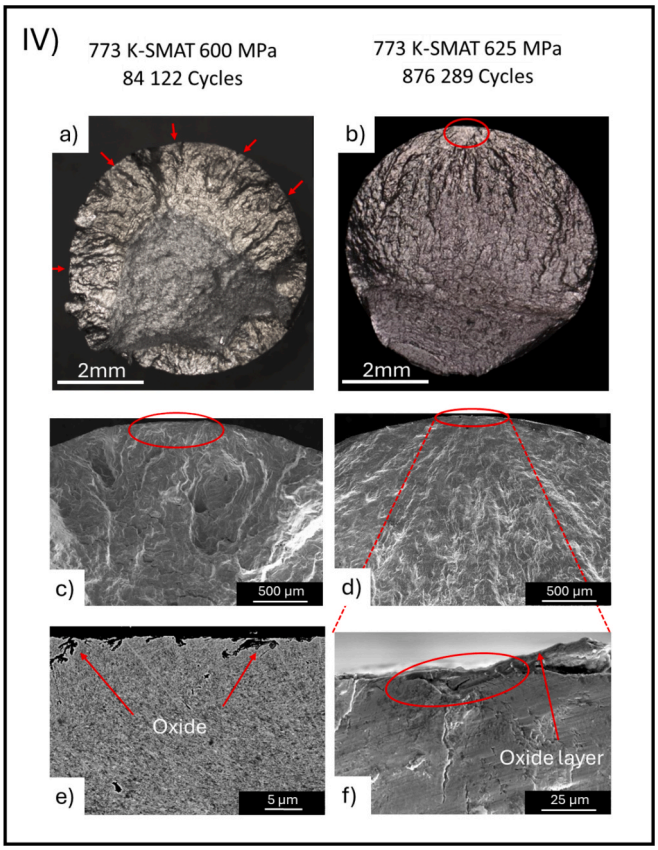

Fig. 8. (*continued*).

nucleation process to subsurface regions at depths of 400–450 µm, i.e., near the tensile peak induced by SMAT (Fig. 6). The linear decrease in stress along the sample radius under rotating bending loading results in a reduction of stress at 400 µm and 450 µm below the surface depth by approximately 13 % and 15 %, respectively, compared to the maximum applied surface stress. Despite the lower intensity of stress fluctuations, cracks nucleated at this location – without the presence of inclusions – most likely due to the high tensile peak in the corresponding regions, on microstructural features similar to those illustrated in Fig. 8 II and III. The microstructural features favouring subsurface crack nucleation in Face Centered Cubic (FCC) materials are usually described as strain localization at crossing micro-shear bands, often near twin boundaries [34], or specific configurations involving significant slip activity [35] such as dislocation substructures or persistent slip bands as reported for SSPD of a 316L [36].

When sample failure occurred at higher stress levels, crack nucleation sites were located on the surface. The fact that the sample survived 10^6 cycles at lower stress intensity proves that no sensitive microstructural features were present around 400 µm below the surface, i.e., within the RS tensile region. Crack nucleation sites were then restricted to the surface defects introduced by SMAT. The fatigue performance of the samples becomes a statistical issue related to the chance to have a microstructural sensitive feature at the location of the tensile residual stress. Based on the present results, the chance to have subsurface crack nucleation sites activated is about 50 % for samples processed at RT and at 523 K (Fig. 7).

The samples processed at 773 K-SMAT present only surface crack nucleation, and high stress levels are necessary to activate them. Based on the residual stress profiles (Fig. 6), the 773 K-SMAT induced a lower surface CRS and a lower tensile peak, located deeper than in the colder conditions (50–100 µm deeper). The lower surface CRS and tensile peak can be attributed to the restoration processes occurring under the 773 K-SMAT. As the tensile peak is present deeper in the sample, the maximal rotating bending stress reached a lower intensity (about 17 % lower than the surface one). These two conditions i) a lower tensile peak value and ii) a lower maximum applied stress, must be sufficient to prevent crack nucleation on sensitive microstructural features, and crack nucleation will rather take place on the surface defects generated by the SMAT process. Although the estimated K_t (2.4) for SMAT at 773 K is similar to the calculated K_t for lower temperatures, this K_t may underestimate the actual surface stress raisers as it does not account for the presence of oxides, pile-ups, or microcracks (Fig. 3e, Fig. 8 IV e-f). These surface features act as notches and negatively affect fatigue performance. Their heterogeneous distribution across the SMAT-treated surface, along with significant variations in size, shape, and severity, introduces local variability in crack nucleation conditions. The morphological diversity of these surface defects alters local stress concentrations and crack nucleation thresholds, thereby contributing to the observed scatter in fatigue life under the 773 K condition (Fig. 7). The surface CRS, even if they are significantly lower than the other conditions (Fig. 6), will delay the propagation. Stress concentrations at these pile-ups and microcracks promote early surface crack nucleation. This suggests that a less intense SMAT condition, achieved through a shorter treatment duration or/and a lower temperature, could optimize fatigue performance by reducing the occurrence and size of surface discontinuities, allowing eventually subsurface crack nucleation to occur in the region where tensile RS are found.

4.2. *Effect of CRS stability on fatigue performance*

Another characteristic of the 773 K-SMAT-treated samples that can explain their higher fatigue performances is the superior stability of the induced CRS. It takes at least 100,000 cycles to start documenting some relaxation process, as shown in Fig. 9; while for the other conditions,

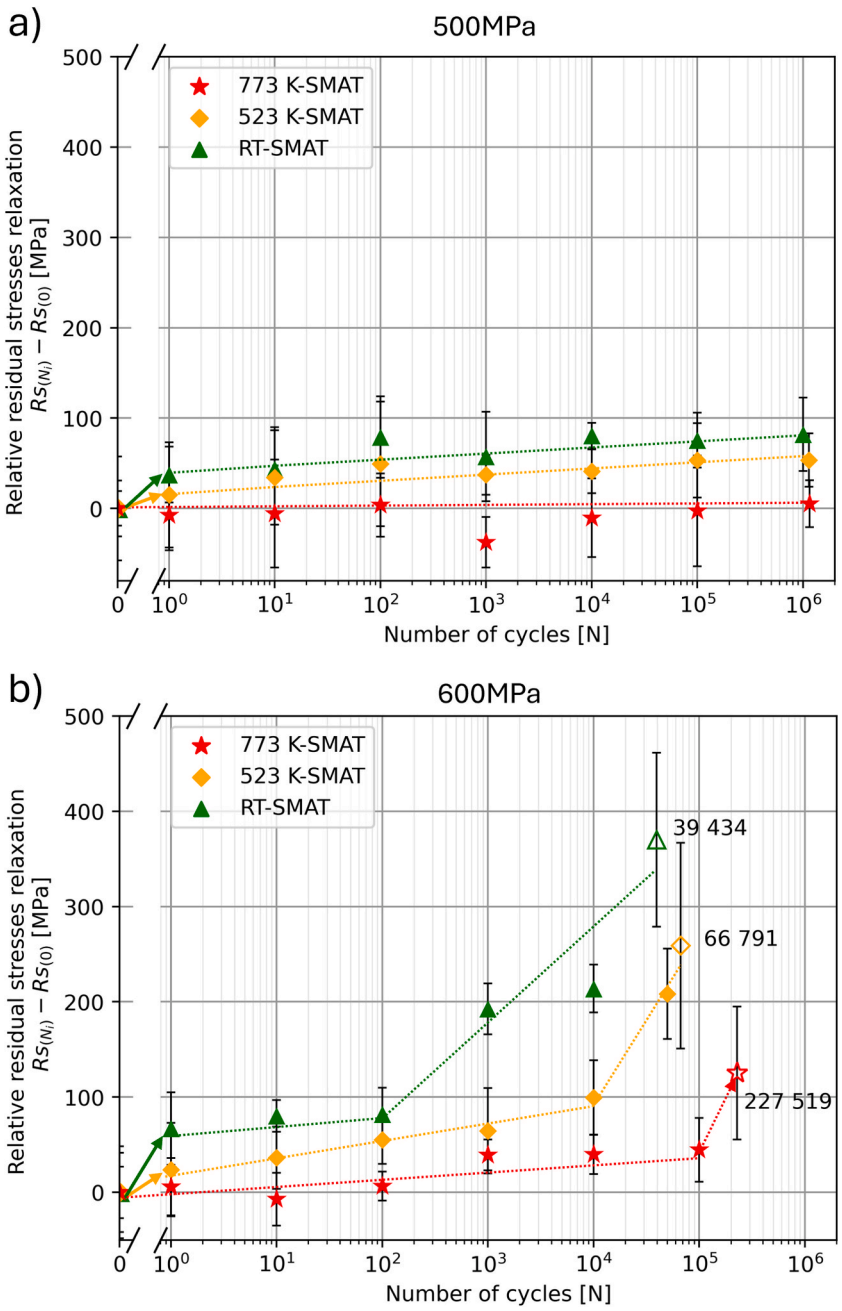

Fig. 9. Relative residual stress relaxations evaluated at a) 500 MPa and b) 600 MPa (hollow markers represent measurements made after fatigue failure). Error bars represent ± 1 standard deviation from the mean value (n = 5).

stress relaxation happens as early as 100 and 10,000 cycles for RT and 523 K conditions, respectively. This stability could be the key factor in enhancing fatigue performance, as it allows the CRS to continuously fulfill their role in delaying crack propagation. Stable surface CRS over numerous cycles is an indication that the microstructure is not sensitive to dynamic softening in the range of applied strains. It is then relevant to question why the microstructure generated at 773 K is more stable than the ones generated at lower temperatures. The enhanced stability of CRS in warm peened (conventional peening or laser shock peening) conditions was already documented and attributed to Dynamic Strain Aging (DSA) and Dynamic Precipitation (DP) mechanisms, as reported in warm peened AISI 4140 steel [37,38], AISI 420 martensitic stainless steel [39], as well as a 304 ASS [40]. However, as 316L presents low interstitial atoms (C, N), DP and DSA mechanisms are expected to be limited. Although DSA has been reported in some studies for the 316L ASS [41–44] where chromium diffusion to dislocation cores was reported at high temperatures (673–923 K) [41,44]. As the 773 K-SMAT took place within this temperature range, chromium diffusion may contribute to the stability of the dislocation structure, preventing any dynamic softening, and be one of the reasons for the good CRS stability for this condition. Under the 773 K-SMAT conditions, DRX occurs too, as evidenced in our previous work [23]. DRX leads the formation of a 30 µm-thick, ductile layer, made of highly recovered ultra-fine-grained (UFG) (Fig. 4). This region has well-organized and recovered dislocation substructures. This has the negative effect of reducing the intensity of the CRS at the surface compared to colder SMAT conditions, but the restored dislocation structures remain more stable as the new dislocations introduced by fatigue solicitations are being generated and moving through the material, preventing dynamic softening and the relaxation of the residual stress. The work-hardening potential of the DRXed

microstructure generated at 773 K can also be documented though the lower surface hardness reported in the 773 K-treated samples (Fig. 5). The UFG microstructures formed by warm SMAT may prevent dynamic softening and impede the propagation of notch and defects present at the sample surface after treatment. The work of Roland et al. [25] demonstrated that annealing treatment performed on RT-SMAT do improve fatigue resistance by 5–6 %, highlighting that recovery which increase ductility and dislocation reorganisation have an effect on fatigue performance. While residual stress stability under fatigue loading was not directly addressed in their study, the present work shows that in the case of 773 K-SMATed samples, the recovery processes generate stable CRS, ultimately enhancing fatigue performance. Although performing SMAT at higher temperatures than RT increases the intensity of associated stress raisers, the DRX and DSA/DP mechanisms active at elevated temperature stabilize the introduced CRS and improve ductility, while reducing the intensity of the tensile peak of the residual stress profile. This combination produced the highest endurance limit in the present work; however, the presence of surface defects generated by the process (microcracks, pile-ups, oxidation) which are acting as a potential site for crack nucleation suggests that the optimal SMAT temperature may lie between 523 K and 773 K or for a shorter process time at 773 K.

4.3. Analysis of fatigue behaviour using a Goodman-type diagram

To better interpret the fatigue performance of 316L stainless steel subjected to SMAT at different temperatures, a Goodman-type diagram [45] was constructed in Fig. 10, considering the local stress at the crack nucleation site for each SMATed condition at 10^6 cycles. These plots consider for each condition the relationship between the applied mean stress and the fatigue stress amplitude normalized by the local hardness at the nucleation site. This hardness normalization allows for a clearer comparison between conditions that induce different hardness levels after SMAT. The applied mean stress corresponds here to the residual stress and two intensities were considered: the one measured after processing the surface (Fig. 10a) and the one after stabilization under fatigue relaxation (Fig. 10b). The fatigue stress amplitude at 10^6 cycles was calculated by considering the local stress at the nucleation site and a concentration factor corresponding to the one associated with the roughness, was considered when crack nucleation took place at the sample surface (K_t value shown in Table 1 for surface crack nucleation and a K_t of 1 for subsurface crack nucleation).

Using the residual stress level after SMAT in the Goodman graph provides some insight into the influence of SMAT conditions on fatigue behaviour (Fig. 10a). For RT and 523 K-SMAT, the points corresponding to surface and subsurface crack nucleation are found in two regions of the graph. Their positions highlight the role of residual stress: at the surface, the presence of high CRS allows for high fatigue stress amplitude, while in depth, the presence of the tensile peak reduce significantly the allowable stress amplitude. Even if the local microstructures differ significantly, the data points from the respective regions lie on a straight line. However, the points corresponding to warm SMAT treatments (shown in red) clearly deviate and appear at a higher position in the diagram. Despite the lower residual stress intensity at the surface and the higher K_t value, the fatigue resistance for the condition processed at 773 K is significantly higher, suggesting that the microstructural modifications generated at the sample surface exhibit better fatigue resistance compared to the colder SMAT conditions.

This approach can be further developed considering the intensity of the stabilized residual stress into the calculation, as plotted in Fig. 10b with the residual stress after fatigue tests at 600 MPa (Fig. 9b). It is important to note that the relaxation behaviour at 600 MPa may not be fully representative of lower applied stresses, such as those leading to fatigue crack initiation at RT and 523 K. However, assuming a similar stabilization mechanism, this approach still provides insight into the influence of residual stress relaxation on fatigue endurance. Further refinement could involve considering relaxation trends at lower loading conditions to improve the accuracy of this analysis. When the stabilized stresses documented Fig. 9b are considered (Fig. 10b), the points corresponding to the surface nucleation at RT and 573 K shift to the right of the Goodman graph as the intensity of CRS decreases. With this shift, a linear trend could emerge between all conditions, suggesting that the endurance limit of SMAT-treated samples at different temperatures could be described using a Goodman-type approach. However, one needs to keep in mind that the local microstructures are quite different, and that further data should be gathered before drawing such a conclusion. The higher position of the point corresponding to the samples SMATed at 773 K in the Goodman graph shows that the stability of its residual stress under fatigue loading for this condition may not be the only reason for it fatigue strength. Despite the lower initial compressive residual stress and the presence of many surface discontinuities that can act as short cracks, this condition resists very well to fatigue solicitations. Based on the linear relationship proposed earlier, one could estimate the applied stress required to initiate a subsurface crack in the 773 K samples. This would correspond to a subsurface crack nucleation at a depth of 450 μm with a tensile residual stress of 50 MPa (resulting in a local stress-to-hardness ratio of about 1.6 MPa.HK^{-1}), giving an estimated fatigue limit of approximately 650 MPa. This represents a 13 % improvement over the current performance driven by surface crack nucleation, underscoring the negative impact of surface discontinuities under the present condition.

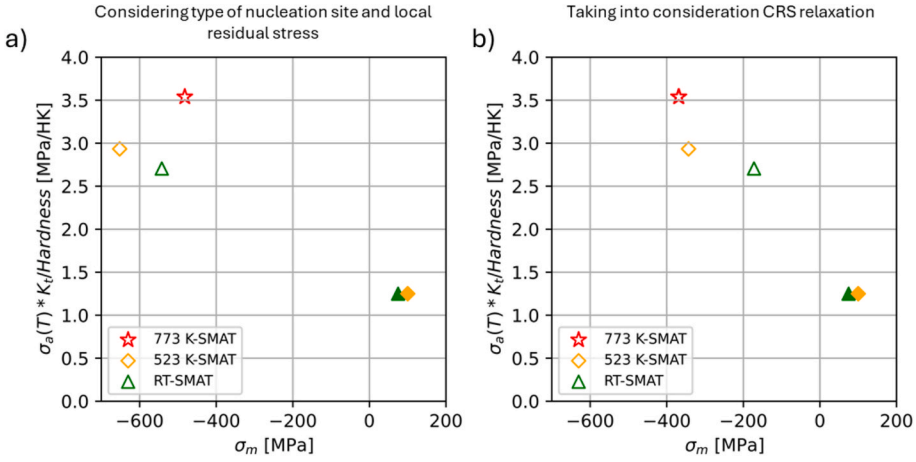

Fig. 10. Goodman diagram of fatigue strength at 10^6 cycles, incorporating the stress intensity factor and local material hardness: a) Considering residual stress before fatigue testing, b) Accounting for residual stress relaxation. hollow markers represent surface crack nucleation sites, and filled markers represent subsurface crack nucleation sites.

To further improve the mechanical properties after SMAT, a processing temperature between 523 K and 773 K could provide the best compromise between introducing high initial CRS, ensuring their stability, and minimizing detrimental surface defects. If such a treatment does not generate detrimental surface discontinuities and leads to a subsurface crack nucleation site located at approximately 400 μm depth with a tensile residual stress of about + 50 MPa, the corresponding local stress-to-hardness ratio would be about 1.5 $MPa{\cdot}HK^{-1}$. This would result in a local stress of 540 MPa, implying an applied stress of approximately 620 MPa − representing an 8 % improvement over the current performance.

5. Conclusions

Surface modifications and microstructural gradients induced by warm SMAT on a 316L ASS were able to significantly improve the fatigue endurance limit at 10^6 cycles. The results highlight the critical role of SMAT temperature on the intensity and stability of the compressive residual stress under cyclic loading and thereby the fatigue performance. The major results can be summarized as follows:

At RT, SMAT effectively eliminates machining grooves and introduces high CRS values, leading to an increase in the fatigue endurance limit compared to the machined condition (+ 25 %). Two types of crack nucleation sites are reported: one related to surface stress raiser and the other related to microstructural features located 400 μm below the surface, corresponding to the tensile peak of residual stress gradient. The competition between surface and subsurface crack initiation depends on the statistical likelihood of a microstructural defect being present within the tensile residual stress region. When such a defect is present, failure occurs at relatively low stress, whereas in its absence, crack nucleation shifts to the surface, where higher stress levels are required for initiation.

At 523 K, the temperature is high enough to activate dynamic recrystallization during SMAT, leading to the formation of a duplex microstructure composed of both recrystallized and deformed fine grains. Although the surface residual stress is slightly higher, and despite the deeper microstructural refinement, no further improvement in fatigue resistance is observed: the endurance limit remains comparable to that of the RT-SMAT condition, with a similar shift from surface to subsurface crack nucleation sites as rupture occurs at lower stress levels.

At 773 K, SMAT generates a highly recovered UFG layer extending over 30 μm beneath the surface. Even if lower compressive residual stress values, higher surface roughness, and the formation of microcracks, pile-ups and an oxidized surface layer are reported, the fatigue performance is further improved by 15 % compared to RT and 523 K. This improvement is attributed to deeper CRS and a lower tensile peak in the RS profile, and a reduced sensibility of the generated microstructure to dynamic softening, i.e., CRS relaxation. The restoration process taking place at 773 K likely led to the formation of a well-organized dislocation network, eventually stabilized by some chromium diffusion to dislocations core due to dynamic strain aging in this temperature range, which has the potential to remain relatively stable under fatigue loading. In other words, the superior work-hardening ability of the UFG layer may prevent dynamic strain softening and significantly delay short crack propagation from the surface discontinuities generated by the SMAT process.

Despite some trade-offs in surface integrity, these results reveal the strong potential of warm SMAT to enhance fatigue performance by generating a microstructure capable of stabilizing the induced compressive residual stress state during fatigue loading. Choosing a SMAT temperature between 523 K and 773 K could lead to further improvement of fatigue performance. A process temperature on the proposed temperature range will offer the advantage to still generate a UFG microstructure with limit oxidation and pile-up formation, preventing the surface to be the weakest point of the material.

CRediT authorship contribution statement

Y Austernaud: Writing – review & editing, Writing – original draft, Methodology, Investigation. **M Novelli:** Writing – review & editing, Writing – original draft, Supervision, Conceptualization. **T Grosdidier:** Writing – review & editing, Writing – original draft, Supervision, Funding acquisition, Conceptualization. **P Bocher:** Writing – review & editing, Writing – original draft, Supervision, Conceptualization.

Declaration of competing interest

The authors declare that they have no known competing financial interests or personal relationships that could have appeared to influence the work reported in this paper.

Acknowledgments

This study was supported in part by the French Government through the program “Investment in the future” operated by the National Research Agency (ANR) and referenced by ANR-11- LABX-0008-01 (Labex DAMAS).

We acknowledge the experimental facilities Procédés | MicroMat from LEM3 (Université de Lorraine - CNRS UMR 7239) » for the SMAT and the microstructural characterization.

Data availability

The data that support the findings of this study are available from the corresponding author upon reasonable request.

References

[1] Maiya PS, Busch DE. Effect of surface roughness on low-cycle fatigue behavior of type 304 stainless steel. Metall Trans A 1975;6:1761–6. https://doi.org/10.1007/BF02642305.
[2] Itoga H, Tokaji K, Nakajima M, Ko H-N. Effect of surface roughness on step-wise *S–N* characteristics in high strength steel. Int J Fatigue 2003;25:379–85. https://doi.org/10.1016/S0142-1123(02)00166-4.
[3] Webster GA, Ezeilo AN. Residual stress distributions and their influence on fatigue lifetimes. Int J Fatigue 2001;23:375–83. https://doi.org/10.1016/S0142-1123(01)00133-5.
[4] Almer JD, Cohen JB, Moran B. The effects of residual macrostresses and microstresses on fatigue crack initiation. Mater Sci Eng A 2000;284:268–79. https://doi.org/10.1016/S0921-5093(99)00779-0.
[5] Li HY, Sun HL, Bowen P, Knott JF. Effects of compressive residual stress on short fatigue crack growth in a nickel-based superalloy. Int J Fatigue 2018;108:53–61. https://doi.org/10.1016/j.ijfatigue.2017.11.010.
[6] Hanlon T, Kwon Y-N, Suresh S. Grain size effects on the fatigue response of nanocrystalline metals. Scr Mater 2003;49:675–80. https://doi.org/10.1016/S1359-6462(03)00393-2.
[7] Mughrabi H, Höppel HW, Kautz M. Fatigue and microstructure of ultrafine-grained metals produced by severe plastic deformation. Scr Mater 2004;51:807–12. https://doi.org/10.1016/j.scriptamat.2004.05.012.
[8] Farrahi GH, Lebrijn JL, Couratin D. Effect of shot peening on residual stress and fatigue life of a spring steel. Fatigue Fract Eng Mat Struct 1995;18:211–20. https://doi.org/10.1111/j.1460-2695.1995.tb00156.x.
[9] Jiang XP, Man C-S, Shepard MJ, Zhai T. Effects of shot-peening and re-shot-peening on four-point bend fatigue behavior of Ti–6Al–4V. Mater Sci Eng A 2007;468–470:137–43. https://doi.org/10.1016/j.msea.2007.01.156.
[10] de los Rios ER, Walley A, Milan MT, Hammersley G. Fatigue crack initiation and propagation on shot-peened surfaces in A316 stainless steel. Int J Fatigue 1995;17:493–9. https://doi.org/10.1016/0142-1123(95)00044-T.
[11] Maleki E, Bagherifard S, Unal O, Bandini M, Farrahi GH, Guagliano M. Introducing gradient severe shot peening as a novel mechanical surface treatment. Sci Rep 2021;11:22035. https://doi.org/10.1038/s41598-021-01152-2.
[12] Lu K, Lu J. Nanostructured surface layer on metallic materials induced by surface mechanical attrition treatment. Mater Sci Eng A 2004;375–377:38–45. https://doi.org/10.1016/j.msea.2003.10.261.
[13] Liu G, Lu J, Lu K. Surface nanocrystallization of 316L stainless steel induced by ultrasonic shot peening. Mater Sci Eng A 2000;286:91–5. https://doi.org/10.1016/S0921-5093(00)00686-9.
[14] Azadmanjiri J, Berndt CC, Kapoor A, Wen C. Development of surface nanocrystallization in alloys by surface mechanical attrition treatment (SMAT). Crit Rev Solid State Mater Sci 2015;40:164–81. https://doi.org/10.1080/10408436.2014.978446.

[15] Grosdidier T, Novelli M. Recent developments in the application of surface mechanical attrition treatments for improved gradient structures: processing parameters and surface reactivity. Mater Trans 2019;60:1344–55. https://doi.org/10.2320/matertrans.MF201929.
[16] Arifvianto B, Suyitno M, Mahardika P, Dewo PT, Iswanto UA. Salim, effect of surface mechanical attrition treatment (SMAT) on microhardness, surface roughness and wettability of AISI 316L. Mater Chem Phys 2011;125:418–26. https://doi.org/10.1016/j.matchemphys.2010.10.038.
[17] Gatey AM, Hosmani SS, Singh RP. Surface mechanical attrition treated AISI 304L steel: role of process parameters. Surf Eng 2016;32:69–78. https://doi.org/10.1179/1743294415Y.0000000056.
[18] Marteau J, Bigerelle M, Mazeran P-E, Bouvier S. Relation between roughness and processing conditions of AISI 316L stainless steel treated by ultrasonic shot peening. Tribol Int 2015;82:319–29. https://doi.org/10.1016/j.triboint.2014.07.013.
[19] Kumar SA, Raman SGS, Narayanan TSNS. Influence of surface mechanical attrition treatment duration on fatigue lives of Ti–6Al–4V. Trans Indian Inst Met 2014;67:137–41. https://doi.org/10.1007/s12666-013-0322-2.
[20] Kumar S, Chattopadhyay K, Singh V. Optimization of the duration of ultrasonic shot peening for enhancement of fatigue life of the alloy Ti-6Al-4V. J Materi Eng Perform 2020;29:1214–24. https://doi.org/10.1007/s11665-020-04661-9.
[21] Novelli M, Bocher P, Grosdidier T. Effect of cryogenic temperatures and processing parameters on gradient-structure of a stainless steel treated by ultrasonic surface mechanical attrition treatment. Mater Charact 2018;139:197–207. https://doi.org/10.1016/j.matchar.2018.02.028.
[22] Maurel P, Weiss L, Bocher P, Grosdidier T. Effects of SMAT at cryogenic and room temperatures on the kink band and martensite formations with associated fatigue resistance in a β-metastable titanium alloy. Mater Sci Eng A 2021;803:140618. https://doi.org/10.1016/j.msea.2020.140618.
[23] Austernaud Y, Novelli M, Bocher P, Grosdidier T. Effect of shot peening temperature on the microstructure induced by surface severe plastic deformation on an austenitic stainless steel. J Mater Process Technol 2025:118823. https://doi.org/10.1016/j.jmatprotec.2025.118823.
[24] Wei P, Hua P, Xia M, Yan K, Lin H, Yi S, et al. Bending fatigue life enhancement of NiTi alloy by pre-strain warm surface mechanical attrition treatment. Acta Mater 2022;240:118269. https://doi.org/10.1016/j.actamat.2022.118269.
[25] Roland T, Retraint D, Lu K, Lu J. Fatigue life improvement through surface nanostructuring of stainless steel by means of surface mechanical attrition treatment. Scr Mater 2006;54:1949–54. https://doi.org/10.1016/j.scriptamat.2006.01.049.
[26] Dureau C, Novelli M, Arzaghi M, Massion R, Bocher P, Nadot Y, et al. On the influence of ultrasonic surface mechanical attrition treatment (SMAT) on the fatigue behavior of the 304L austenitic stainless steel. Metals 2020;10. https://doi.org/10.3390/met10010100.
[27] Novelli M, Fundenberger J-J, Bocher P, Grosdidier T. On the effectiveness of surface severe plastic deformation by shot peening at cryogenic temperature. Appl Surf Sci 2016;389:1169–74. https://doi.org/10.1016/j.apsusc.2016.08.009.
[28] Dureau C, Arzaghi M, Massion R, Nadot Y, Grosdidier T. On the high cycle fatigue resistance of austenitic stainless steels with surface gradient microstructures: effect of load ratio and associated residual stress modification. Mater Sci Eng A 2022;840:142916. https://doi.org/10.1016/j.msea.2022.142916.
[29] ASTM 91A., A guide for fatigue testing and the statistical analysis of fatigue data ». In ASTM Special Technical Publication No. 91-A, (1963).
[30] Li JK, Mei Y, Duo W, Renzhi W. An analysis of stress concentrations caused by shot peening and its application in predicting fatigue strength. Fatig. Fract. Eng. Mater. Struct. 1992;15:1271–9. https://doi.org/10.1111/j.1460-2695.1992.tb01262.x.
[31] D. Delbergue, D. Texier, M. Levesque, P. Bocher, Comparison of Two X-Ray Residual Stress Measurement Methods: Sin2 ψ and Cos α, Through the Determination of a Martensitic Steel X-Ray Elastic Constant, in: Residual Stresses 2016: ICRS-10, Sydney, Australia, 2016: pp. 55–60. Doi: 10.21741/9781945291173-10.
[32] Moore MG, Evans WP. Mathematical correction for stress in removed layers in X-ray diffraction residual stress analysis. SAE Trans 1958;66:340–5.
[33] B. Beausir, J.-J. Fundenberger, Analysis Tools for Electron and X-ray diffraction, ATEX, (2017). www.atex-software.eu.
[34] Ghosh S, Bibhanshu N, Suwas S, Chatterjee K. Micro-mechanisms underlying enhanced fatigue life of additively manufactured 316L stainless steel with a gradient heterogeneous microstructure. Mater Sci Eng A 2023;886:145665. https://doi.org/10.1016/j.msea.2023.145665.
[35] Stein CA, Cerrone A, Ozturk T, Lee S, Kenesei P, Tucker H, et al. Fatigue crack initiation, slip localization and twin boundaries in a nickel-based superalloy. Curr Opin Solid State Mater Sci 2014;18:244–52. https://doi.org/10.1016/j.cossms.2014.06.001.
[36] Huang HW, Wang ZB, Lu J, Lu K. Fatigue behaviors of AISI 316L stainless steel with a gradient nanostructured surface layer. Acta Mater 2015;87:150–60. https://doi.org/10.1016/j.actamat.2014.12.057.
[37] R. Menig, V. Schulze, O. Vöhringer, Residual Stress Relaxation and Fatigue Strength of AISI 4140 under Torsional Loading after Conventional Shot Peening, Stress Peening and Warm Peening, in: L. Wagner (Ed.), Shot Peening, Wiley-VCH Verlag GmbH & Co. KGaA, Weinheim, FRG, 2006: pp. 311–316. Doi: 10.1002/3527606580.ch39.
[38] Ye C, Suslov S, Kim BJ, Stach EA, Cheng GJ. Fatigue performance improvement in AISI 4140 steel by dynamic strain aging and dynamic precipitation during warm laser shock peening. Acta Mater 2011;59:1014–25. https://doi.org/10.1016/j.actamat.2010.10.032.
[39] Angkurarach L, Juijerm P. Effects of high-temperature deep rolling on fatigue, work hardening, and residual stress relaxation of martensitic stainless steel AISI 420. J Mater Eng Perform 2020;29:1416–23. https://doi.org/10.1007/s11665-020-04656-6.
[40] Nikitin I, Scholtes B. Deep rolling of austenitic steel AISI 304 at different temperatures – near surface microstructures and fatigue. HTM J. Heat Treat. Mater. 2012;67:188–94. https://doi.org/10.3139/105.110152.
[41] Hong S-G, Lee K-O, Lee S-B. Dynamic strain aging effect on the fatigue resistance of type 316L stainless steel. Int J Fatigue 2005;27:1420–4. https://doi.org/10.1016/j.ijfatigue.2005.06.037.
[42] Li B, Zheng Y, Zhao J, Shi S, Zhang Z, Chen X. Cyclic deformation behavior and dynamic strain aging of 316LN stainless steel under low cycle fatigue loadings at 550 °C. Mater Sci Eng A 2021;818:141411. https://doi.org/10.1016/j.msea.2021.141411.
[43] Sarkar A, Nagesha A, Sandhya R, Laha K, Okazaki M. Manifestations of dynamic strain aging under low and high cycle fatigue in a type 316LN stainless steel. Mater High Temp 2018;35:523–8. https://doi.org/10.1080/09603409.2017.1404684.
[44] Samuel KG, Mannan SL, Rodriguez P. Serrated yielding in AISI 316 stainless steel. Acta Metall 1988;36:2323–7. https://doi.org/10.1016/0001-6160(88)90331-8.
[45] Nicholas T, Zuiker JR. On the use of the Goodman diagram for high cycle fatigue design. Int J Fract 1996;80:219–35. https://doi.org/10.1007/BF00012670.